

UCC Library and UCC researchers have made this item openly available. Please [let us know](#) how this has helped you. Thanks!

Title	Hydrokinetic energy exploitation under combined river and tidal flow
Author(s)	Fouz, D. M.; Carballo, Rodrigo; Ramos, V.; Iglesias, Gregorio
Publication date	2019-05-11
Original citation	Fouz, D. M., Carballo, R., Ramos, V. and Iglesias, G. (2019) 'Hydrokinetic energy exploitation under combined river and tidal flow', Renewable Energy, 143, pp. 558-568. doi: 10.1016/j.renene.2019.05.035
Type of publication	Article (peer-reviewed)
Link to publisher's version	http://www.sciencedirect.com/science/article/pii/S0960148119306949 http://dx.doi.org/10.1016/j.renene.2019.05.035 Access to the full text of the published version may require a subscription.
Rights	© 2019 Elsevier Ltd. All rights reserved. This manuscript version is made available under the CC-BY-NC-ND 4.0 license http://creativecommons.org/licenses/by-nc-nd/4.0/
Embargo information	Access to this article is restricted until 24 months after publication by request of the publisher.
Embargo lift date	2021-05-11
Item downloaded from	http://hdl.handle.net/10468/8200

Downloaded on 2021-11-27T07:43:33Z

1 Hydrokinetic energy exploitation under combined river and tidal flow

2 D.M. Fouz¹, R. Carballo^{1*}, V. Ramos², G. Iglesias^{3, 4}

3 ¹*Univ. de Santiago de Compostela, Área de Ingeniería Hidráulica, EPSE, Campus Univ. s/n, 27002 Lugo, Spain*

4 ²*Interdisciplinary Centre of Marine and Environmental Research of the University of Porto, Terminal de Cruzeiros*
5 *do Porto de Leixões, Avenida General Norton de Matos, S/N, 4450-208 Matosinhos, Portugal*

6 ³*MaREI, Environmental Research Institute & School of Engineering, University College Cork, Ireland*

7 ⁴*School of Engineering, University of Plymouth, UK*

8

9 **Abstract**

10 Hydrokinetic energy has been mainly studied in areas where the principal driver of the current is
11 the tide. However, in certain areas river discharges play also a principal role. The exploitation of
12 the hydrokinetic resource in such areas has its own peculiarities, dictated by the combined
13 influence of the two driving agents. The objective of this paper is to investigate the exploitation
14 of hydrokinetic energy in the Miño Estuary, the largest estuary in NW Spain and N Portugal,
15 with a focus on the site-specific performance of hydrokinetic energy converters (HECs) and its
16 intra-annual variability. A state-of-the-art hydrodynamics numerical model is implemented and
17 successfully validated based on field data. A third-generation HEC—to be more specific, the
18 new Smart Freestream Turbine (SFT)—is considered, and its performance at the location with
19 the greatest potential is assessed by means of: (i) site-specific efficiency, (ii) availability factor,
20 and (iii) capacity factor. We find that, whereas the site-specific efficiency does not vary
21 significantly, the availability and capacity factors do experience substantial intra-annual
22 (seasonal) variability. In summer and autumn, river discharges are low, and the tide dominates
23 the hydrokinetic resource. In contrast, during winter and spring, the river discharges
24 significantly contribute to the resource, leading to a considerable increase in the availability and
25 capacity factors. More generally, the results imply that in areas subject to combined fluvial and
26 tidal influences the performance of HECs may depart significantly from that in tide-dominated
27 areas, and this departure must be carefully weighed in assessing a project.

28

29 **Keywords:** hydrokinetic energy; tidal stream energy; river discharge; seasonal variability;
30 hydrokinetic energy converter

*Corresponding author

E-mail address: rodrigo.carballo@usc.es

31 **1. Introduction**

32 Global warming has drawn attention to new renewable ways of energy production based on
33 principles of efficiency and sustainability [1]. As a result, hydrokinetic energy has been
34 postulated as one of the most promising renewable energy sources that can be developed in the
35 medium term due to its high potential and its reduced environmental impact [2-6].

36 The hydrokinetic resource is the result of different factors, namely: tidal currents, ocean
37 currents, barotropic flows resulting from river discharges and baroclinic circulation, amongst
38 others. The viability of its exploitation requires that peak velocities attain $1\text{-}1.5\text{ ms}^{-1}$ [7]. As a
39 result, estuarine areas have emerged as a promising site for the exploitation of hydrokinetic
40 energy, primarily resulting from the action of the tide which is enhanced by the complex
41 geometry of semi-enclosed bodies [8-10]. Nevertheless, the influence of large river discharges
42 on the available resource and their interaction with tidal flows have not been appropriately
43 investigated.

44 On the other hand, the hydrokinetic resource can be harnessed by the so-called Hydrokinetic
45 Energy Converters (HECs). According to the International Electrotechnical Commission (IEC)
46 criterion, HECs can be classified in five main groups [11-15]: (i) devices with horizontal axis
47 parallel to flow, (ii) devices with horizontal axis perpendicular to flow, (iii) devices with vertical
48 axis, (iv) hydrofoils and (v) other devices. HECs are still currently under development and, as it
49 is the case of other marine renewables [16,17], they are expected to become more economically
50 competitive. Recently, a new generation of HECs has been developed, the so-called third
51 generation devices [18], designed to operate in shallow areas with relatively low velocities and
52 reduced depths (roughly 0.7 ms^{-1} of velocity magnitude and 1 m depth) —where hydrokinetic
53 energy exploitation was not previously considered— and allowing the reduction of the
54 environmental impact by using a compact generation equipment.

55 Planning of a new hydrokinetic energy farm should rely on the selection of the optimum device-
56 location combination, which in turn should consider several aspects [19-21], as it is the case of
57 other marine renewables [22-24]. This is of paramount importance in shallow areas with narrow
58 sections given that, in addition to energy production considerations, the geometry imposes

59 strong limitations to turbine installation and operation [25-27]. In this context, the Galician
60 coast is characterized by a number of estuaries with complex geometry and, in some cases,
61 substantial freshwater discharges. River Miño is the most important fluvial course in this region.
62 Its estuary, with its main axis (Figures 1 and 2) extending over approximately 38 km [28] has a
63 total area of about 23 km² and an average depth of about 2.6 m [29]. The tidal regime is purely
64 semidiurnal, with a form factor [30] $F = 0.0932$ and a maximum tidal range of approximately
65 4.0 m (mesotidal). The estuarine circulation will be shown to be profoundly influenced by the
66 river discharge. The annual discharge is roughly 400 m³s⁻¹, ranging from monthly minima of
67 100 m³s⁻¹ to monthly maxima of 1000 m³s⁻¹. As a result of the action of the two major
68 hydrodynamic forcing factors (the tide and freshwater discharges) over its narrow and shallow
69 sections, this estuary presents significant current velocities, well in excess of 1 ms⁻¹, and
70 therefore constitutes a hotspot for hydrokinetic energy exploitation [31].

71

72

[FIGURE 1]

73

74

[FIGURE 2]

75

76 In this work, the hydrokinetic resource exploitation in the Miño Estuary is analysed by
77 considering the installation of a Smart Freestream Turbine (SFT). For this purpose, and
78 considering the high variability in the freshwater discharge, which may be expected to affect the
79 intra-annual performance of the SFT, the intra-annual spatio-temporal distribution of the current
80 velocities is computed by implementing a shallow-water numerical model. Then, by combining
81 the velocity data obtained by the numerical model with the power curve of the device, the intra-
82 annual energy production of SFT at three locations of interest [31] is computed (Figure 2).
83 Finally, having determined the SFT-site combination providing the largest energy production
84 amongst those previously selected, its performance is thoroughly analysed through a gamut of
85 performance parameters.

86 This paper is structured as follows: first, in Section 2, the methodology used in this work for
 87 assessing the resource distribution and analysing the performance of the HEC selected is
 88 thoroughly described; then, in Section 3, the results are presented and discussed focusing on
 89 three main aspects: resource assessment, site selection and performance analysis; finally, in
 90 Section 4, the major findings and conclusions are presented.

91

92 **2. Material and methods**

93 *2.1. Numerical model formulation*

94 The first step prior to proposing alternatives for installing a hydrokinetic turbine is to
 95 thoroughly analyse the space-time distribution of the available resource. To this end, the
 96 Delft3D FLOW model [32] is implemented for the Miño Estuary and validated by means of
 97 field data. The model solves the Navier-Stokes equations under the shallow-water and
 98 Boussinesq assumptions coupled to the transport equation, thereby allowing the computation of
 99 both the barotropic and baroclinic circulation. The equations are solved in their 2DH form
 100 [33,34]:

101

$$\frac{\partial \zeta}{\partial t} + \frac{\partial[(d + \zeta)U]}{\partial x} + \frac{\partial[(d + \zeta)V]}{\partial y} = Q, \quad (1)$$

$$\left. \begin{aligned} \frac{\partial U}{\partial t} + U \frac{\partial U}{\partial x} + V \frac{\partial U}{\partial y} - fV &= -g \frac{\partial \zeta}{\partial x} - \frac{g}{\rho_0} \int_{-d}^{\zeta} \frac{\partial \rho'}{\partial x} dz + \frac{\tau_{xx} - \tau_{bx}}{\rho_0(d + \zeta)} + \nu_h \nabla^2 U \\ \frac{\partial U}{\partial t} + U \frac{\partial V}{\partial x} + V \frac{\partial V}{\partial y} + fU &= -g \frac{\partial \zeta}{\partial y} - \frac{g}{\rho_0} \int_{-d}^{\zeta} \frac{\partial \rho'}{\partial y} dz + \frac{\tau_{yy} - \tau_{by}}{\rho_0(d + \zeta)} + \nu_h \nabla^2 V \end{aligned} \right\}, \text{ and} \quad (2)$$

$$\frac{\partial(\zeta + d)c}{\partial t} + \frac{\partial[(\zeta + d)Uc]}{\partial x} + \frac{\partial[(\zeta + d)Vc]}{\partial y} = D_h \nabla^2 c - \lambda_d (d + \zeta)c + R, \quad (3)$$

102

103 where (1) represents the conservation of mass under Boussinesq's hypothesis; the pair of
 104 equations (2) express the conservation of momentum along x and y directions; and (3) is the
 105 transport equation, which is solved for temperature and salinity. In these equations ζ and d

106 represent the water levels and depth, respectively; u and v are the components of the velocity in
107 the directions x and y respectively; ρ and ρ_0 express the density and reference density of sea
108 water respectively; Q is the intensity of mass sources; f stands for the Coriolis parameter; ν_h is
109 the horizontal eddy viscosity; τ_{bx} and τ_{by} are the shear stress components over the sea bottom,
110 and τ_{sx} and τ_{sy} the wind stress components on the sea surface; c represents the temperature or
111 salinity constituents; D_h is the horizontal eddy diffusivity; λ_d represents the decay processes of
112 first-order; finally, R stands for the source term.

113 Regarding the spatial discretisation, the model uses the Arakawa-C grid, consisting in a
114 staggered grid within which ζ is defined at grid cell centres, and u and v are determined at the
115 central points of the grid cell faces. With respect to the discretisation of the horizontal advection
116 terms, the Cyclic method is applied. Finally, temporal discretisation is carried out by using a
117 semi-implicit alternating direction implicit (ADI) algorithm.

118

119 *2.2. Numerical model implementation*

120 The finite difference mesh is a Cartesian grid with a spatial resolution of 100 x 100 m which
121 covers the whole estuary, including the intertidal zones and emerged areas, and extends offshore
122 up to a water depth of approximately 100 m. In this manner the outer boundary is far enough
123 that eventual numerical disturbances do not affect the study area (Figure 3). The model is run
124 with a time step of 1 minute, which according to the Courant–Friedrichs–Levy criterion is
125 sufficient to ensure numerical stability considering the mesh resolution adopted [35].

126

127 [FIGURE 3]

128

129 The bathymetry, kindly provided by Hydrographic Institute of the Navy, was complemented
130 with a digital terrain model with a resolution of 50 x 50 m commissioned by the Galician
131 Regional Government (Xunta de Galicia), which allowed the representation of the intertidal
132 areas. The accurate representation of shallow areas is of key importance given the sensitivity of
133 the hydrokinetic resource to variations in the water depth and geomorphological configuration

134 [36]. Figure 4 shows the bathymetry and topographic data as interpolated onto the
135 computational grid in the study area.

136

137 [FIGURE 4]

138

139 The oceanic open boundaries comprise the north, south and west limits of the grid, along which
140 the main harmonics [37] of the astronomical tide (Table 1) and the salinity and temperature of
141 the oceanic waters are imposed through Dirichlet boundary conditions. The freshwater input of
142 the River Miño is imposed at the inner estuary, defined by its total discharge along with salinity
143 and temperature characteristics.

144

145 [TABLE 1]

146

147 Previous works [31] have shown that the discharge of the River Miño presents a markedly
148 seasonal behaviour. On this basis, four case studies are defined based on the variability of the
149 flow discharge as provided by the Miño-Sil Hydrographic Confederation for an average year
150 (Table 2).

151

152 [TABLE 2]

153

154 In order to analyse the seasonal hydrodynamics, the model is used to simulate the
155 aforementioned four seasonal scenarios by considering the average characteristics of the
156 relevant forcing factors during each of these four periods. In addition, in order to capture the
157 variability resulting from the tide within each case, the model is run during a 14.75 day period
158 [33,35] (half synodic month), i.e., a complete spring-neap tidal cycle, preceded by an additional
159 spin-up period [38].

160

161 *2.3. Numerical model validation*

162 With the aim of validating the numerical model, computed velocity measurements are compared
 163 with field data recorded by an Acoustic Doppler Current Profiler (ADCP) during a period of
 164 approximately 22 days. Before comparing computed and measured data, observed velocities are
 165 de-noised and vertically averaged by means of a Stationary Wavelet Transformation (SWT) of
 166 db10 type belonging to Daubechies family [39-42]. Figure 5 shows the comparison between
 167 simulated and measured data. Overall, the model accurately reproduces the hydrodynamics of
 168 the estuary, with a high determination coefficient, $R^2=0.85$. In particular, the model captures the
 169 variation induced by the action of the tide, with downstream and upstream velocities
 170 corresponding to positive and negative values, respectively, along with the flow induced by the
 171 river which leads to a significant asymmetry in the resulting currents.

172

[FIGURE 5]

174

175 *2.4. Hydrokinetic energy resource and HEC performance assessment*

176 The available power density from the kinetic energy of the water flowing through a vertical
 177 cross-section perpendicular to flow direction per unit of time $p_{KE}(t)$ is given by [33]:

178

$$p_{KE}(t) = \frac{1}{2} \rho \alpha(t) [V(t)]^3 \quad (4)$$

179

180 where ρ represents the water density; $V(t)$ is the flow velocity averaged over the section per unit
 181 of time; finally, $\alpha(t)$ is the energy coefficient which takes into account the velocity dispersions
 182 through the water column being usually set as $\alpha(t) \approx 1$ [43].

183 The electrical energy output of a HEC, E_e , over a period of time, T , can be obtained by
 184 integrating the power density over the period of interest as [35]:

185

$$E_e = \int_0^T AC_p p_{KE}(t) dt \quad (5)$$

186

187 where C_p is the power coefficient which represents the relationship between power available
 188 and harnessed [44]; finally, A is the swept area.

189 It is important to consider that the above equations (Eq. 4 and Eq. 5) are theoretical expressions.
 190 Real HECs only work within a specific range of velocities with a lower velocity threshold or
 191 cut-in, V_{ci} , and upper threshold or cut-off, V_{co} [35]. The efficiency of HECs is provided by
 192 device developers through its power curve. The main technical specifications and power curve
 193 of SFT are shown in Table 3 and Figure 6, respectively.

194

195 [TABLE 3]

196

197 [FIGURE 6]

198

199 As a result, the energy output of the SFT-site combinations selected is straightforwardly
 200 computed by combining the current velocity results obtained at the locations of interest and the
 201 power curve of the SFT. As expressed in Eq. 5 the electrical energy output, E_e , is determined by
 202 integrating the power output data with respect to time, which is computed for the four case
 203 studies, each of them covering a 14.75-day period. Annual figures are obtained by considering
 204 that the intra-seasonal resource distribution is appropriately characterized by the fortnightly
 205 period, i.e.:

206

$$(E_{e,season})_i = \frac{(E_{e,simulation})_i}{T_{simulation}} T_{season} \quad (6)$$

$$E_{e,annual} = \sum_{i=1}^4 (E_{e,season})_i \quad (7)$$

207

208 where $(E_{e,season})_i$ is the seasonal energy production for the i season; $(E_{e,simulation})_i$ represents the
 209 energy production during the 14.75-day simulation period for the i season; $T_{simulation}$ expresses

210 the duration of the simulation period, i.e., 14.75 days; T_{season} stands for the duration of a natural
211 season; finally, $E_{e,annual}$ is the annual energy output.

212 Based on previous works [35,45-47], three performance parameters are selected for the analysis
213 of the SFT-site combination providing the largest amount of energy: (i) the site-specific
214 efficiency, (ii) the availability factor and (iii) the capacity factor.

215 The site-specific efficiency, η_e , was defined in previous work [35] as the ratio between the
216 electrical energy output, E_e , and the available energy at the site, E , over a reference period of
217 time:

218

$$\eta_e = \frac{E_e}{E} \quad (8)$$

219

220 The availability factor, A_f , is the ratio between the operation time, t_o (during which the flow
221 speed is between the cut-in and cut-off velocities of the HEC) and the total period considered, T
222 [46]:

223

224

$$A_f = \frac{t_o}{T} \quad (9)$$

225

226 Finally, the capacity factor, C_f , is the ratio between the electrical energy output of a device over
227 a given period, E_e , and the electrical energy output it would have produced, had it operated at its
228 nominal regime during the same period [47]:

229

$$C_f = \frac{E_e}{TP_R} \quad (10)$$

230

231 where T is the duration of the reference period and P_R is the rated electrical power of the device.

232

233 **3. Results and discussion**

234 *3.1. Resource assessment*

235 Once validated, the numerical model can be used to compute the flow throughout the estuary.
236 For this purpose, and in order to quantify the hydrokinetic resource and the influence of the
237 fresh water discharge, the model is run considering the combined effect of the main forcing
238 factors as defined in Section 2. The analysis of the results is focused on three specific sites of
239 interest for energy exploitation: Area I in the middle estuary and Areas II and III in the inner
240 estuary (Figure 2) [31].

241 Given that the aim of this work is to quantify the hydrokinetic energy production in the areas
242 proposed—and the influence of fluvial discharges on it—the numerical model was applied to
243 compute the flow patterns during a spring-neap tidal cycle for the four case studies defined
244 (Section 2); the results are presented in Figures 7, 8 and 9 for Areas I, II and III, respectively.
245 The highest velocities occur during winter, the season with the largest freshwater discharge,
246 with a gradual and significant reduction from spring to autumn due to the reduction in
247 freshwater discharges. The influence of the river inputs is clearly observed in winter, during
248 which upstream velocities virtually disappear. The gradual reduction in the river discharge
249 allows upstream velocities to develop, as is apparent from the presence of a clear second peak in
250 each tidal cycle in summer and autumn of almost the same intensity as during the ebb.

251

252 [FIGURE 7]

253

254 [FIGURE 8]

255

256 [FIGURE 9]

257

258 From the analysis of the variations in the flow speed in the three areas selected, the following
259 results are obtained. The largest reduction in flow speed from one season to the next, hereinafter
260 referred to as *seasonal reduction*, occurs from winter to spring, with average values of 0.40

261 ms^{-1} , 0.50 ms^{-1} and 0.35 ms^{-1} in Areas I, II and III, respectively, closely followed by spring and
262 summer seasons, with mean *seasonal reductions* of 0.20 ms^{-1} , 0.40 ms^{-1} and 0.33 ms^{-1} in Areas
263 I, II and III, respectively. In contrast, the *seasonal reduction* from summer to autumn is almost
264 negligible: 0.01 ms^{-1} , 0.02 ms^{-1} and 0.02 ms^{-1} for Areas I, II and III, respectively. These trends
265 are caused by the intra-annual reductions in freshwater discharges, roughly of $450 \text{ m}^3\text{s}^{-1}$ from
266 winter to spring, $400 \text{ m}^3\text{s}^{-1}$ from spring to summer, and $45 \text{ m}^3\text{s}^{-1}$ from summer to autumn (i.e.,
267 approx. a reduction of 44%, 69% and 26%, respectively). In addition, it can be observed that
268 the geometrical characteristics lead to a different reduction in the magnitude of the currents
269 amongst the areas considered, the section with largest modifications being the narrowest (≈ 165
270 m).

271 The aforementioned seasonal variations in flow speed result in large seasonal variations in the
272 available power density (Eq. 5). In Figure 10, the seasonal power density is plotted for the area
273 with the greatest resource (Area II). In accordance with the seasonal distribution of fluvial
274 contributions and resulting current velocities, winter is the most energetic season, reaching
275 values of up to 3.46 kWm^{-2} , with an average of 2.14 kWm^{-2} ; in spring, the reduction in the
276 velocity magnitude results in a significant decrease in the power density with an average value
277 of 0.80 kWm^{-2} ; finally, in summer and autumn the power density plummets due to the sharp
278 reduction in the river discharges, both seasons presenting similar figures: 0.22 kWm^{-2} and 0.19
279 kWm^{-2} , respectively.

280

281 [FIGURE 10]

282

283 3.2. Site selection

284 The energy production of the SFT at the locations of interest is computed by combining the
285 velocity magnitude results with the power curve of the turbine (Section 2) (Figure 11). As can
286 be observed, the greatest energy output would be obtained in Area II, with an annual figure of
287 2.26 MWh, considerably higher than that in Area III (0.96 MWh) and tripling the value of Area
288 I (0.73 MWh). Furthermore, the differences in energy production between areas differ markedly

289 during the year. The greatest differences are present in winter with a total energy production of
290 1.46 MWh, 0.62 MWh and 0.51 MWh at Areas II, III and I, respectively. In spring, a significant
291 reduction in the energy production relative to the winter values occurs with total figures of 0.53
292 MWh, 0.26 MWh and 0.19 MWh at Areas II, III and I, respectively; thereby the differences
293 between areas are accordingly smaller. Finally, in summer and autumn the energy output
294 plummets, with each season representing in all cases less than 10% of the production attained in
295 winter, and less than 30% of spring (e.g., the energy production during autumn at Area I would
296 be 1.39% of the winter figure).

297 On the bases of these results, Area II emerges as the site with the greatest potential for installing
298 a hydrokinetic turbine and therefore is retained for a thorough performance assessment.

299

300

[FIGURE 11]

301

302 *3.3. Site-specific performance assessment*

303 The following performance parameters of the SFT at Area II were computed: availability factor,
304 A_f , capacity factor, C_f , and site-specific efficiency, η_{ss} , (Section 2), based on the intra-annual
305 energy output results (Figure 12).

306

307

[FIGURE 12]

308

309 The good match between the operation requirements of the turbine and Area II, in particular its
310 low cut-in velocity (0.7 ms^{-1}), leads to high values of the availability factor throughout the year:
311 100% in winter, 73.89% in spring, 49.86% summer, and 48.06% in autumn. These figures
312 reflect the importance of the large river discharge in winter for the turbine performance,
313 generating outflow currents in excess of 0.8 ms^{-1} throughout winter (even during the flood tide),
314 and thus above the cut-in speed (0.7 ms^{-1}). The average annual availability factor is 67.95%,
315 which corresponds to a total of 5871 hours of operational time in a year.

316 On the other hand, the capacity factor, C_f , is the parameter most influenced by the seasonality:
317 60.15% in winter, 22.06% in spring, 6.22% in summer, and 5.00% in autumn. From these
318 values, the equivalent hours, E_h , (hours of energy production at nominal power) [35] are:
319 1299.24 h in winter, 476.50 h in spring, 134.35 h in summer, and 107.78 h in autumn. As a
320 result, and despite the low levels attained over the second half of the year (summer-autumn), an
321 annual value of 23.35% for the capacity factor, i.e., 2017 h of E_h , is achieved. These values are
322 considered acceptable in the case of other renewables (e.g., $C_f > 20\%$ in wind energy) [48,49].
323 Finally, the site-specific turbine efficiency presents a completely different behaviour, with little
324 seasonal variability: 40.18% in winter, 39.44% in spring, 40.16% in summer, 37.52% in
325 autumn, meaning that the level of adequacy of the turbine for the site is roughly similar
326 throughout the year.

327

328 **3. Conclusions**

329 The hydrokinetic resource in many coastal areas is not only the result of the tide, but also of
330 other factors such as river discharges. As a case study of a fluvio-tidal coastal area, the Miño
331 Estuary was considered in this work. With this aim, a shallow-water numerical model of the
332 estuarine hydrodynamics, successfully validated against field measurements, was used to
333 investigate the exploitation of the hydrokinetic resource in the estuary.

334 Three sites (Areas I, II and III) were initially selected as suitable for installing a third-generation
335 SFT. The hydrological regime was found to produce a substantial seasonal variability. During
336 winter and spring river discharges dominate the hydrodynamics, to the point of precluding the
337 upstream flow during the flood throughout winter. In contrast, during summer and autumn, the
338 reduction in freshwater discharges allows the tide to dominate the hydrodynamics. Then, the
339 corresponding distribution of the power density was computed. It was found that the available
340 resource experiences a significant intra-annual variation with average power density values
341 during winter approximately ten times higher than during summer and autumn.

342 The most appropriate area for installing a hydrokinetic turbine amongst the three areas retained
343 (I, II and III) was selected based on their seasonal energy production values. The largest energy

344 production can be obtained in Area II, almost doubling the energy output of Areas I and III; the
345 seasonality, however, is considerable, with winter providing the lion's share of the energy
346 production.

347 Finally, the intra-annual figures of several performance parameters of interest for the SFT-Area
348 II combination were computed. All in all, from the results it can be concluded that the
349 hydrodynamic regime of Area II is suited to the characteristics of the turbine selected, for which
350 river discharges play a major role. In particular, its low cut-in velocity (0.7 ms^{-1}) leads to high
351 values of the availability factor throughout the year, with an average annual figure of 67.95%
352 and 100% in winter. Large river discharges during the rainy season (in winter and, to a lesser
353 extent, spring) result in downstream currents above the cut-in velocity even during the flood
354 tide, leading to high availability factors and, in general, good performance figures.

355 In sum, the results obtained indicate that in areas subject to both tidal effects and large river
356 discharges, the performance of HECs may differ significantly from tide-dominated areas, with a
357 substantial intra-annual variability that needs to be accounted for in planning the exploitation of
358 the resource.

359

360 **Acknowledgements**

361 This paper has been conducted in the framework of the Research Project *Consolidación e*
362 *estructuración* – 2016 CIGEO (Ref ED431B 2019/30) supported by Xunta de Galicia. The
363 authors are grateful to the Instituto Hidrográfico de Portugal and to the Confederación
364 Hidrográfica del Miño-Sil for providing the ADCP and river discharge data, respectively.

365

366 **References**

367 [1] World Commission on Environment and Development (WCED). Our Common Future.
368 1987.

369 [2] Aghsaee P, Markfort CD. Effects of flow depth variations on the wake recovery behind a
370 horizontal-axis hydrokinetic in-stream turbine. *Renewable Energy* 2018;125:620-9.

- 371 [3] Els RHv, Junior ACPB. The Brazilian Experience with Hydrokinetic Turbines. Energy
372 Procedia 2015;75:259-64.
- 373 [4] Ramos V, Carballo R, Sanchez M, Veigas M, Iglesias G. Tidal stream energy impacts on
374 estuarine circulation. Energy Conversion and Management 2014;80:137-49.
- 375 [5] Petrie J, Diplas P, Gutierrez M, Nam S. Characterizing the mean flow field in rivers for
376 resource and environmental impact assessments of hydrokinetic energy generation sites.
377 Renewable Energy 2014;69:393-401.
- 378 [6] Holanda PdS, Blanco CJC, Mesquita ALA, Brasil Junior ACP, de Figueiredo NM, Macêdo
379 EN et al. Assessment of hydrokinetic energy resources downstream of hydropower plants.
380 Renewable Energy 2017;101:1203-14.
- 381 [7] European Commission. The exploitation of tidal marine currents. 1996;EUR16683EN.
- 382 [8] Zarzuelo C, López-Ruiz A, Díez-Minguito M, Ortega-Sánchez M. Tidal and subtidal
383 hydrodynamics and energetics in a constricted estuary. Estuarine, Coastal and Shelf Science
384 2017;185:55-68.
- 385 [9] Riglin J, Daskiran C, Jonas J, Schleicher WC, Oztekin A. Hydrokinetic turbine array
386 characteristics for river applications and spatially restricted flows. Renewable Energy
387 2016;97:274-83.
- 388 [10] Garcia Novo P, Kyojuka Y. Analysis of turbulence and extreme current velocity values in
389 a tidal channel. J Marine Sci Technol 2018.
- 390 [11] Segura E, Morales R, Somolinos JA, López A. Techno-economic challenges of tidal energy
391 conversion systems: Current status and trends. Renewable and Sustainable Energy Reviews
392 2017;77:536-50.
- 393 [12] King J, Tryfonas T. Tidal stream power technology - state of the art. Proceedings of IEEE
394 OCEANS 2009 - EUROPE Conference 2009:1-8.
- 395 [13] Núñez LR, López A, Somolinos JA. The GESMEY Project. Design and Development of a
396 Second Generation TEC. Proceedings of the 9th European Wave and Tidal Energy Conference
397 (EWTEC11) 2011.

398 [14] International Electrotechnical Commission. IEC-TC214, Technical Specification: Marine
399 energy. Wave, tidal and other water current converters. Part 1: Terminology. IEC/TS 62600-1.
400 2011;1.0.

401 [15] Barbarelli S, Amelio M, Castiglione T, Florio G, Scornaienchi NM, Cutrupi A et al.
402 Analysis of the equilibrium conditions of a double rotor turbine prototype designed for the
403 exploitation of the tidal currents. *Energy Conversion and Management* 2014;87:1124-33.

404 [16] Rezanejad K, Guedes Soares C, López I, Carballo R. Experimental and numerical
405 investigation of the hydrodynamic performance of an oscillating water column wave energy
406 converter. *Renewable Energy* 2017;106:1-16.

407 [17] Vicinanza D, Contestabile P, Quvang Harck Nørgaard J, Lykke Andersen T. Innovative
408 rubble mound breakwaters for overtopping wave energy conversion. *Coastal Engineering*
409 2014;88:154-70.

410 [18] López A, Somolinos JA, Núñez LR. Modelado Energético de Convertidores Primarios para
411 el Aprovechamiento de las Energías Renovables Marinas. *Revista Iberoamericana de*
412 *Automática e Informática Industrial RIAI* 2014;11:224-35.

413 [19] Wang W, Yin R, Yan Y. Design and prediction hydrodynamic performance of horizontal
414 axis micro-hydrokinetic river turbine. *Renewable Energy* 2019;133:91-102.

415 [20] Li Y, Lence BJ, Calisal SM. An integrated model for estimating energy cost of a tidal
416 current turbine farm. *Energy Conversion and Management* 2011;52:1677-87.

417 [21] Garcia Novo P, Kyojuka Y, Ginzo Villamayor MJ. Evaluation of turbulence-related high-
418 frequency tidal current velocity fluctuation. *Renewable Energy* 2019;139:313-25.

419 [22] Arean N, Carballo R, Iglesias G. An integrated approach for the installation of a wave
420 farm. *Energy* 2017;138:910-9.

421 [23] Vicinanza D, Contestabile P, Ferrante V. Wave energy potential in the north-west of
422 Sardinia (Italy). *Renewable Energy* 2013;50:506-21.

423 [24] Weiss CVC, Ondiviela B, Guinda X, del Jesus F, González J, Guanche R et al. Co-location
424 opportunities for renewable energies and aquaculture facilities in the Canary Archipelago.
425 *Ocean & Coastal Management* 2018.

- 426 [25] Álvarez M, Carballo R, Ramos V, Iglesias G. An integrated approach for the planning of
427 dredging operations in estuaries. *Ocean Engineering* 2017;140:73-83.
- 428 [26] González-Caballín JM, Álvarez E, Gutiérrez-Trashorras AJ, Navarro-Manso A, Fernández
429 J, Blanco E. Tidal current energy potential assessment by a two dimensional computational fluid
430 dynamics model: The case of Avilés port (Spain). *Energy Conversion and Management*
431 2016;119:239-45.
- 432 [27] Garcia-Oliva M, Djordjević S, Tabor GR. The influence of channel geometry on tidal
433 energy extraction in estuaries. *Renewable Energy* 2017;101:514-25.
- 434 [28] Sousa R, Guilhermino L, Antunes C. Molluscan fauna in the freshwater tidal area of the
435 River Minho estuary, NW of Iberian Peninsula. *International Journal of Limnology*
436 2005;41(2):141-7.
- 437 [29] Freitas V, Costa-Dias S, Campos J, Bio A, Santos P, Antunes C. Patterns in abundance and
438 distribution of juvenile flounder *Platichthys flesus*, in Minho estuary (NW Iberian Peninsula).
439 *Aquatic Ecology* 2009;43:1143.
- 440 [30] Pugh DT. *Tides, Surges, and Mean Sea-Level/a Handbook for Engineers and Scientists.* :
441 John Wiley & Sons Inc, 1996.
- 442 [31] Fouz DM, Carballo R, Iglesias G. Tidal stream energy production in estuarine areas: A
443 case study in NW Spain. *Abstract Volume Campus do Mar International Science Conference*
444 2018 2018:24.
- 445 [32] Deltares. *User Manual Delft3D-FLOW.* Deltares ed. Delft, The Netherlands, 2010.
- 446 [33] Carballo R, Iglesias G, Castro A. Numerical model evaluation of tidal stream energy
447 resources in the Ría de Muros (NW Spain). *Renewable Energy* 2009;34:1517-24.
- 448 [34] Blunden LS, Bahaj AS. Initial evaluation of tidal stream energy resources at Portland Bill,
449 UK. *Renewable Energy* 2006;31:121-32.
- 450 [35] Ramos V, Iglesias G. Performance assessment of Tidal Stream Turbines: A parametric
451 approach. *Energy Conversion and Management* 2013;69:49-57.
- 452 [36] Zarzuelo C, López-Ruiz A, Ortega-Sánchez M. Impact of human interventions on tidal
453 stream power: The case of Cádiz Bay. *Energy* 2018;145:88-104.

454 [37] Le Provost C, Bennett AF, Cartwright DE. Ocean tides for and from Topex/Poseidon.
455 Science 1995;267:639-47.

456 [38] Iglesias G, Sánchez M, Carballo R, Fernández H. The TSE index – A new tool for selecting
457 tidal stream sites in depth-limited regions. Renewable Energy 2012;48:350-7.

458 [39] Iglesias G, Carballo R. Seasonality of the circulation in the Ría de Muros (NW Spain). J
459 Mar Syst 2009;78:94-108.

460 [40] Loutas TH, Sotiriades G, Kostopoulos V. On the application of wavelet transform of AE
461 signals from composite materials. 2004:433-45.

462 [41] Daubechies I. Orthonormal bases of compactly supported wavelets. Communications in
463 Pure and Applied Mathematics 1988;XLI:901-96.

464 [42] Hu X-, Liu LT, Ducarme B, Hsu HT, Sun H-. Wavelet filter analysis of local atmospheric
465 pressure effects in the long-period tidal bands. Phys Earth Planet Inter 2006;159:59-70.

466 [43] Chow VT. Open-channel hydraulics. New York: McGraw-Hill, 1959.

467 [44] Bahaj AS. Generating electricity from the oceans. Renewable and Sustainable Energy
468 Reviews 2011;15:3399-416.

469 [45] Ramos V, Carballo R, Álvarez M, Sánchez M, Iglesias G. A port towards energy self-
470 sufficiency using tidal stream power. Energy 2014;71:432-44.

471 [46] Chang T, Wu Y, Hsu H, Chu C, Liao C. Assessment of wind characteristics and wind
472 turbine characteristics in Taiwan. Renewable Energy 2003;28:851-71.

473 [47] Carballo R, Iglesias G. A methodology to determine the power performance of wave
474 energy converters at a particular coastal location. Energy Conversion and Management
475 2012;61:8-18.

476 [48] Boccard N. Capacity factor of wind power realized values vs. estimates. Energy Policy
477 2009;37:2679-88.

478 [49] Nemes C, Munteanu F. The wind energy system performance overview: Capacity factor vs.
479 technical efficiency. Int J Math Models Methods Appl Sci 2011;5:159-66.

480

481 **Figure captions**

482 Figure 1. Location of the Miño Estuary on the Galician coast, NW Spain.

483 Figure 2. Miño Estuary, study area and ADCP location.

484 Figure 3. Area covered by the model grid.

485 Figure 4. Bathymetry and topographic configuration of the Miño Estuary as interpolated to
486 model grid.

487 Figure 5. Magnitude of current velocities measured by the ADCP (circles) and computed by the
488 model (line) projected along the main axis of the estuary during the validation period.

489 Figure 6. Power curve of SFT.

490 Figure 7. Magnitude of the current velocity at Area I throughout a 14.75-day spring-neap cycle
491 in the winter, spring, summer and autumn cases.

492 Figure 8. Magnitude of the current velocity at Area II throughout a 14.75-day spring-neap cycle
493 in the winter, spring, summer and autumn cases.

494 Figure 9. Magnitude of the current velocity at Area III throughout a 14.75-day spring-neap cycle
495 in the winter, spring, summer and autumn cases.

496 Figure 10. Power density at Area II throughout a 14.75-day spring-neap cycle in the winter,
497 spring, summer and autumn cases.

498 Figure 11. Annual electric energy output of SFT at Areas I, II and III.

499 Figure 12. Performance of SFT at Area II in terms of availability factor, capacity factor and site-
500 specific turbine efficiency.

Table 1. Tidal constituents at the ocean boundary of the grid.

Constituent	Amplitude (m)	Phase (°)
M2	1.0654	76.5400
S2	0.3700	105.9200
N2	0.2251	57.5200
K2	0.1017	102.1200
K1	0.0743	66.2800
O1	0.0595	320.7100
P1	0.0215	57.5100
Q1	0.0195	265.4700
Z0	2.0687	0.0000

Table 2. Case studies.

Season	Months	Average discharge (m ³ s ⁻¹)	Average temperature (°C)
Winter	January	1013.25	10.9
	February		
	March		
Spring	April	568.47	14.5
	May		
	June		
Summer	July	174.09	20.5
	August		
	September		
Autumn	October	129.21	14.9
	November		
	December		

Table 3. Main technical specifications of SFT [D (m), rotor diameter; A (m^2), swept area; W (kg), turbine weight; V_{ci} (ms^{-1}), cut-in velocity; V_{co} (ms^{-1}), cut-off velocity; V_R (ms^{-1}), rated velocity; P_R (kW), rated power; L (m), device length; B (m), device width; H (m), device height; N , number of blades; ω (rpm), angular velocity].

Smart Freestream turbine			
D (m)	1.0	P_R (kW)	1.12
A (m^2)	0.8	L (m)	2.6
W (kg)	300.0	B (m)	1.1
V_{ci} (ms^{-1})	0.7	H (m)	1.1
V_{co} (ms^{-1})	3.1	N	3.0
V_R (ms^{-1})	2.0	ω (rpm)	90-230

Figure 1

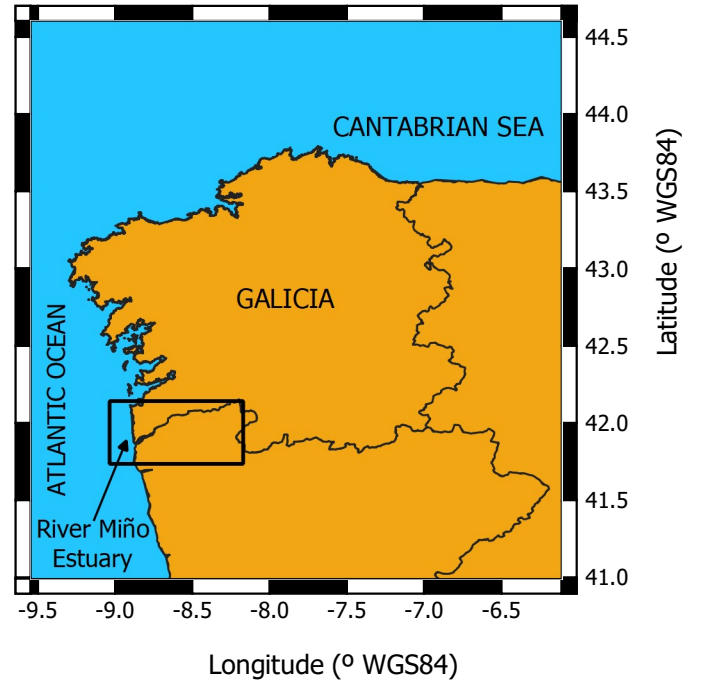
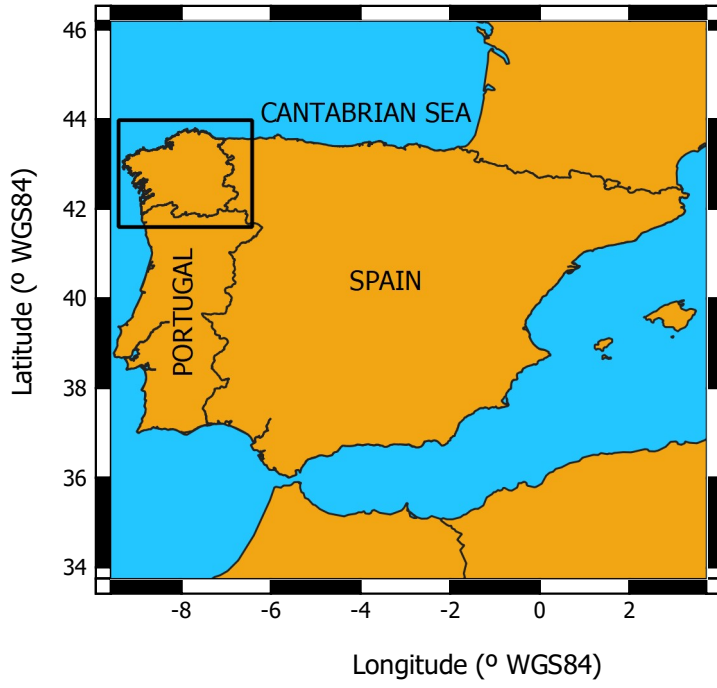


Figure 2

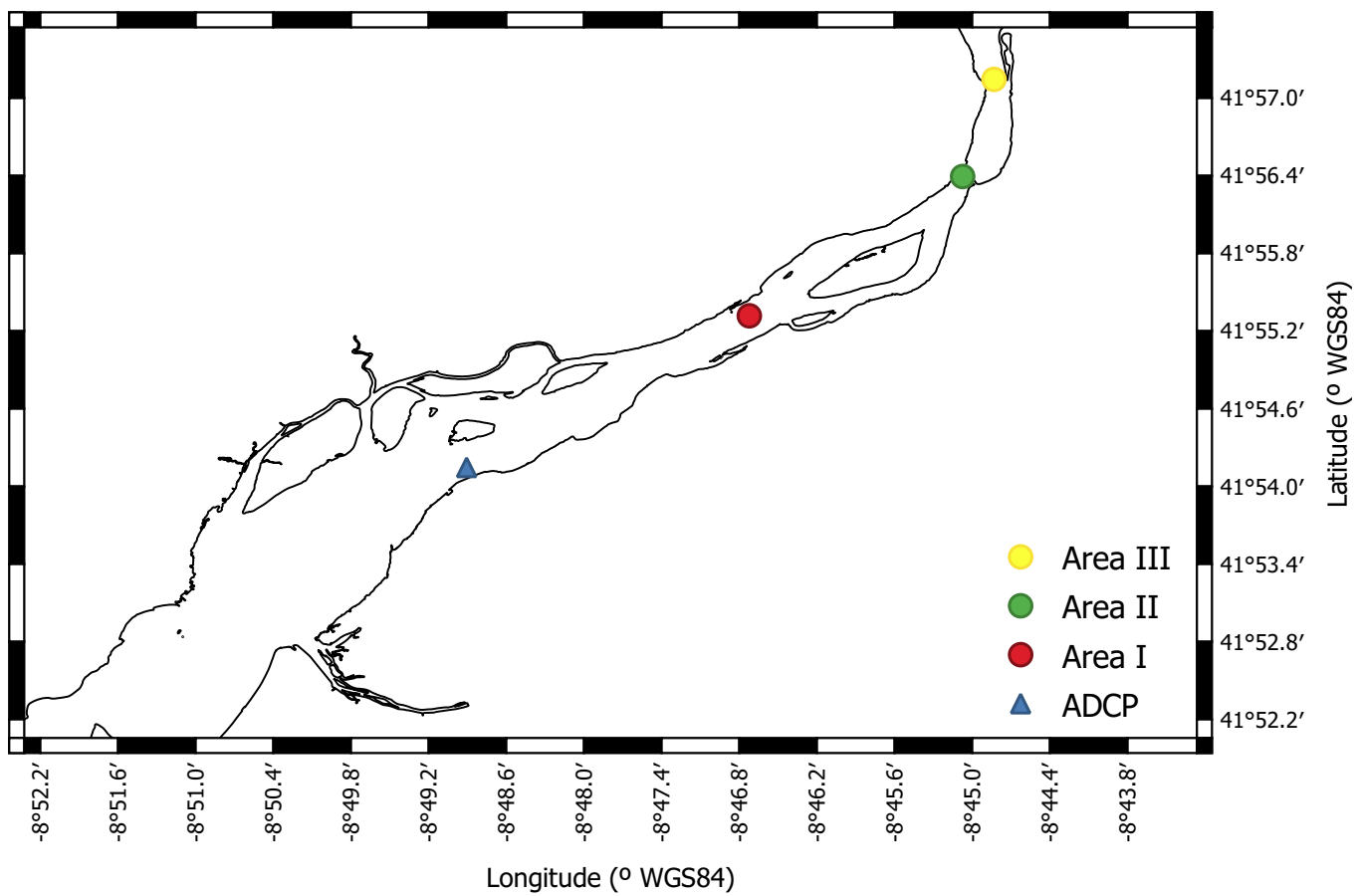


Figure 3

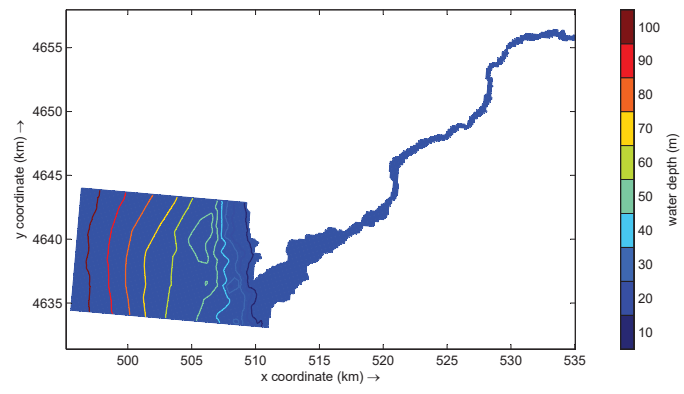


Figure 4

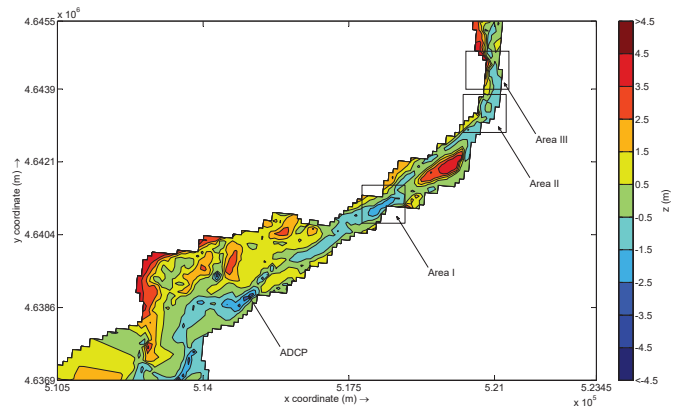


Figure 5

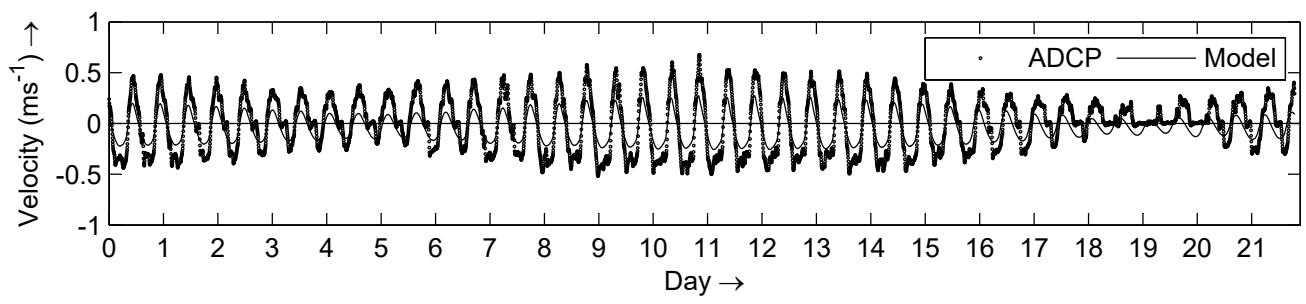


Figure 6

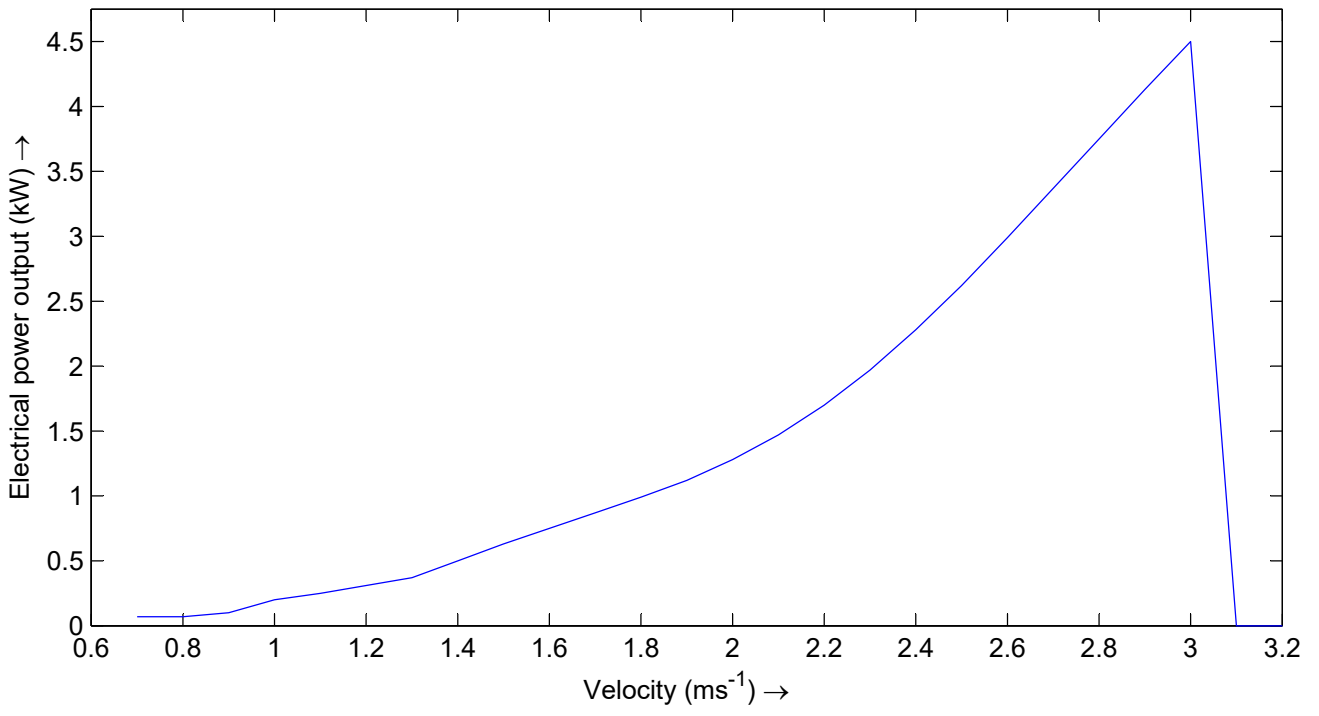


Figure 7

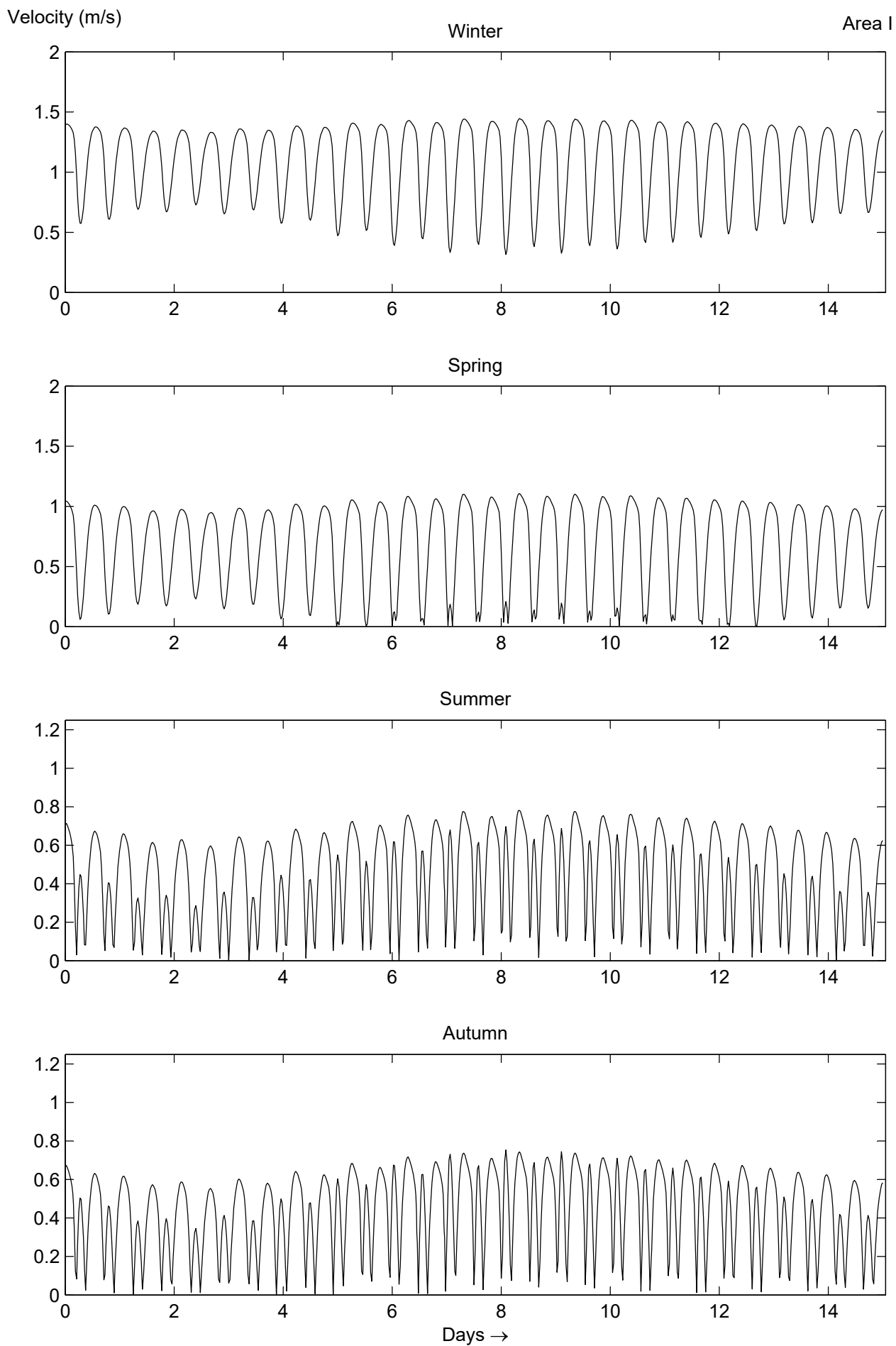


Figure 8

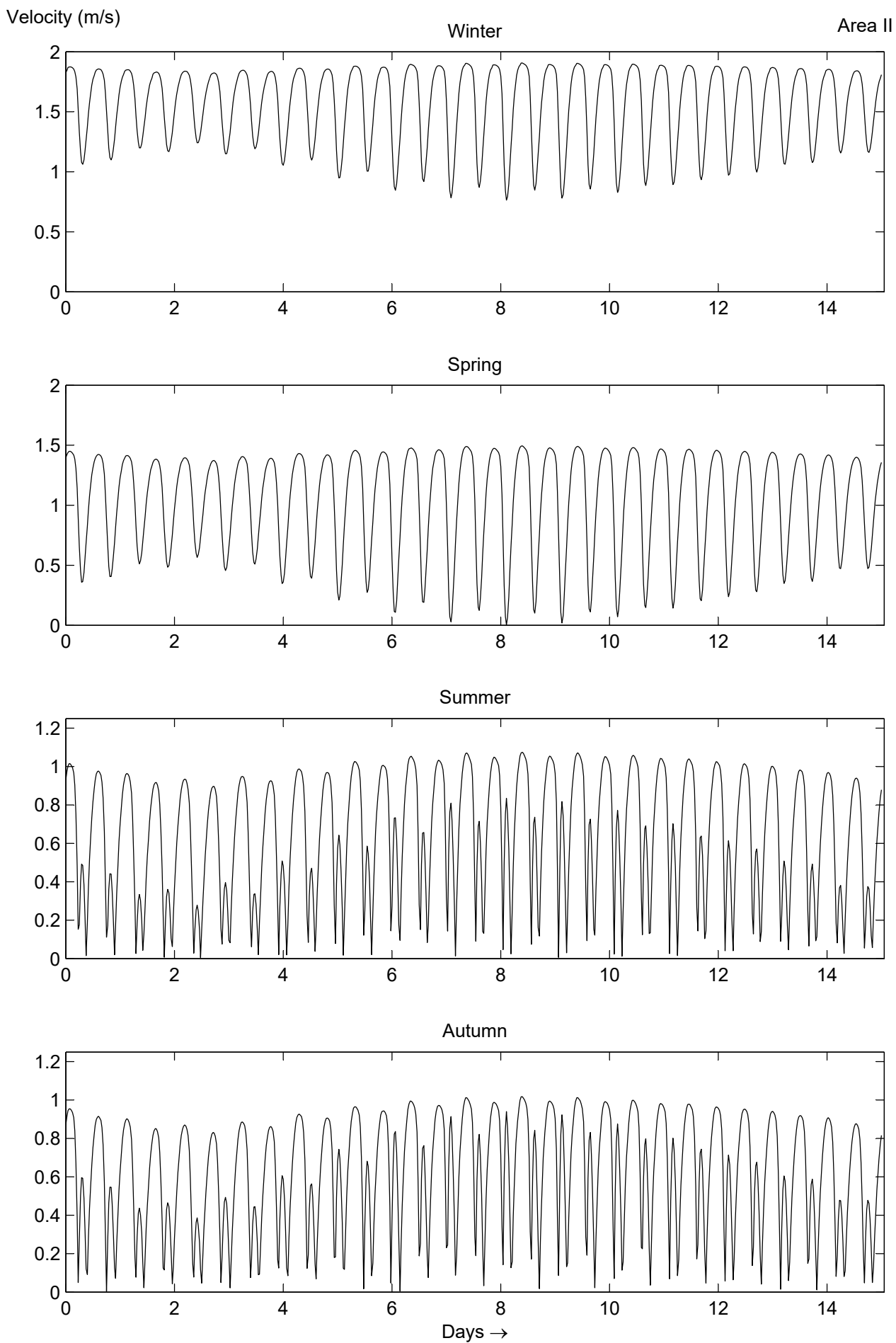


Figure 9

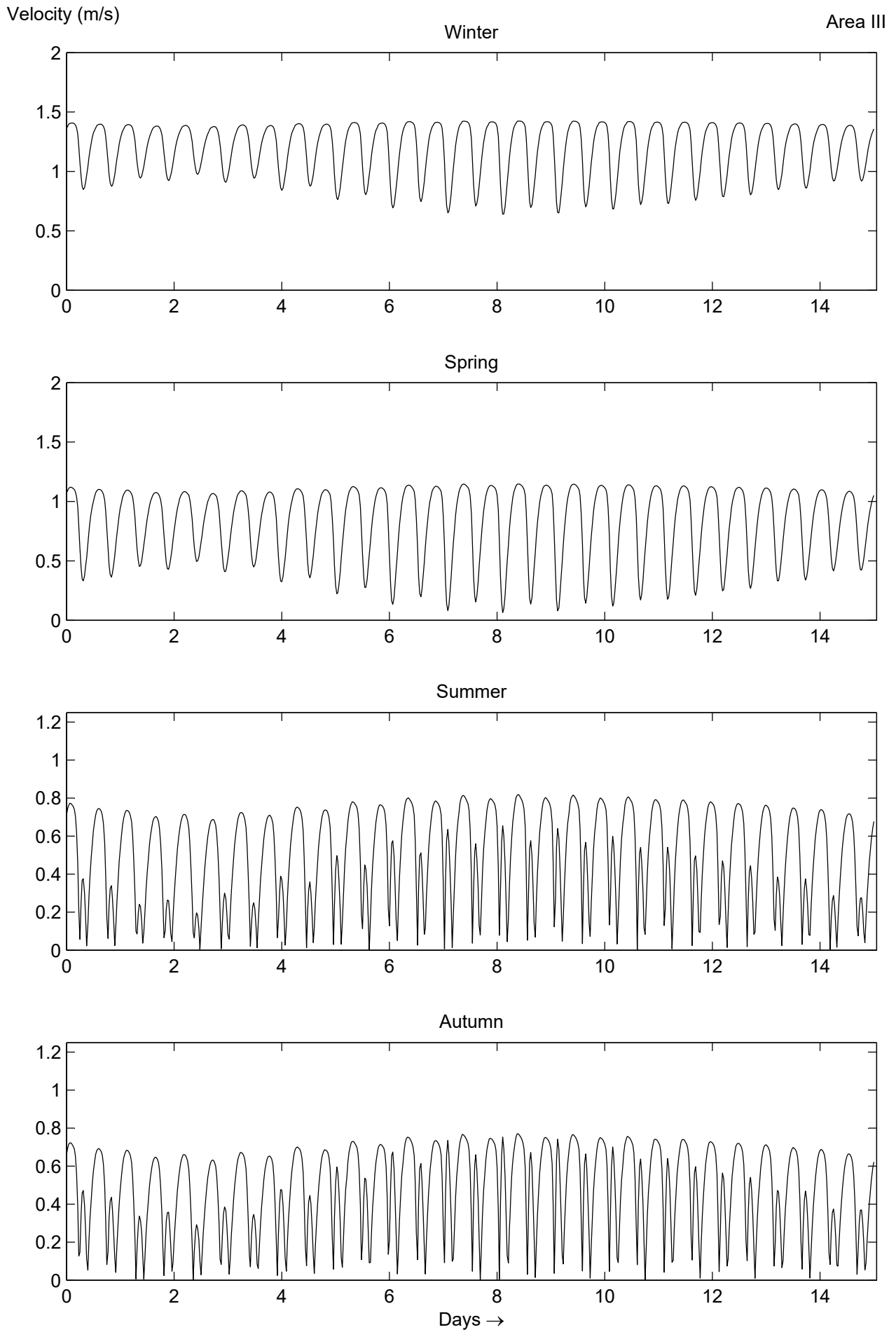


Figure 10

Power Density (kWm^{-2})

Area II

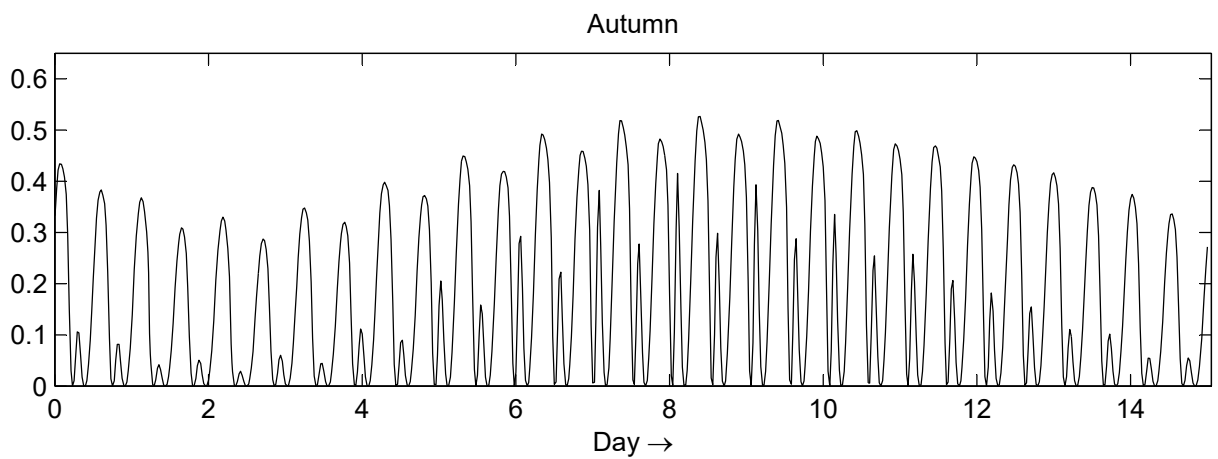
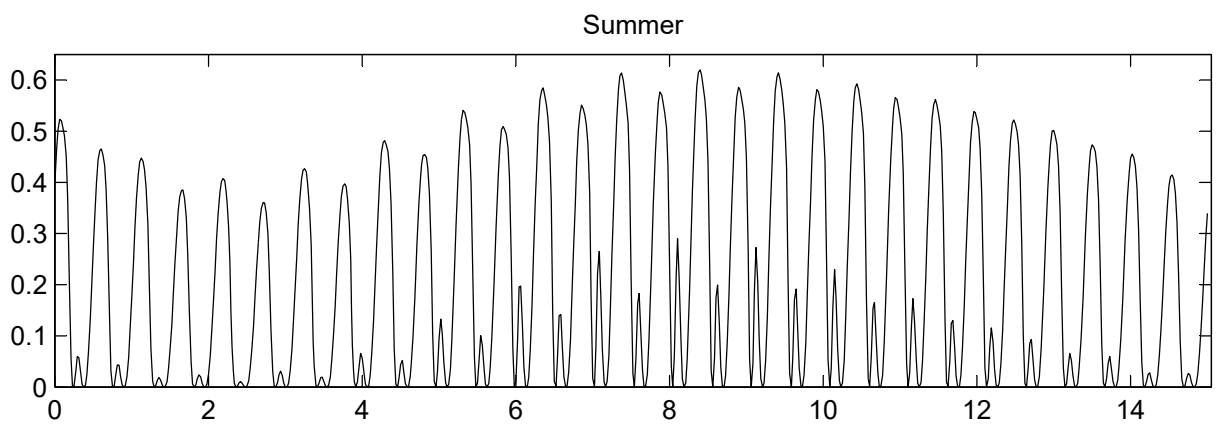
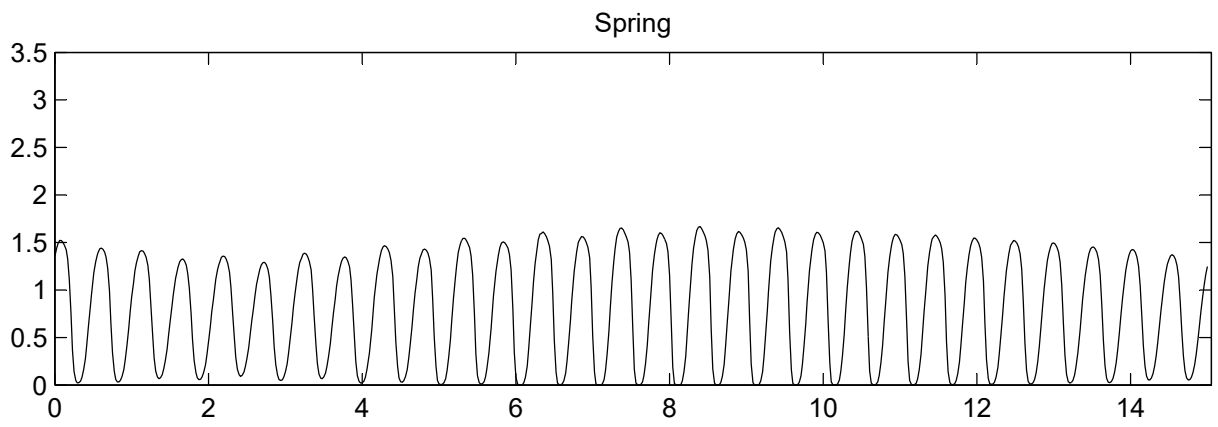
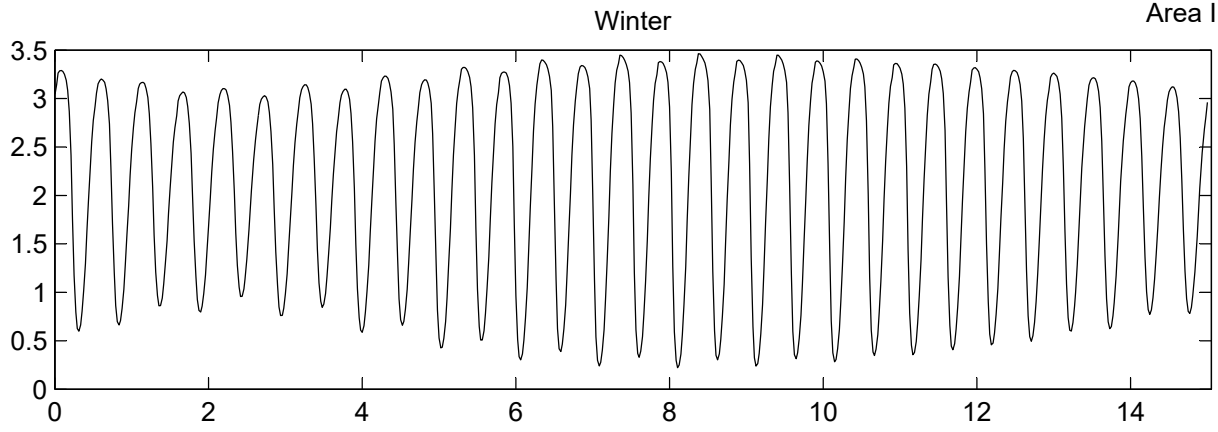


Figure 11

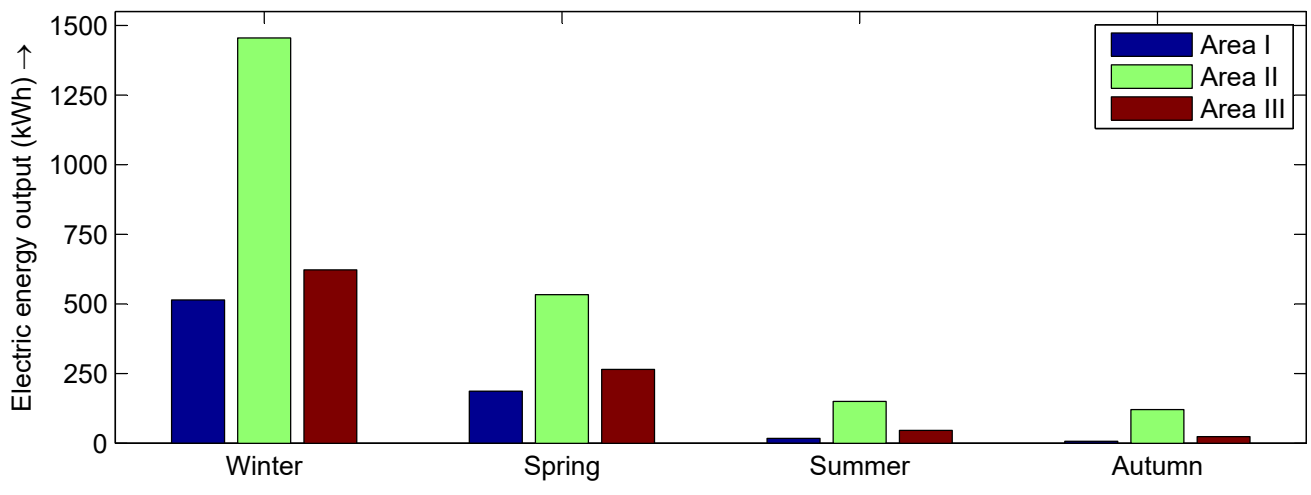


Figure 12

